

Research Article

Mechanical Characteristics and Energy Evolution of Sandstone Three-Point Bending Test

Tao Qin , Kai Ren , Zhi Liu , Yan-Wei Duan , and Lei Wang 

Key Laboratory of Mining Engineering, Heilongjiang Universities, Heilongjiang University of Science and Technology, Harbin 150022, China

Correspondence should be addressed to Kai Ren; 19140270@qq.com

Received 26 September 2021; Accepted 15 November 2021; Published 8 December 2021

Academic Editor: Bin Gong

Copyright © 2021 Tao Qin et al. This is an open access article distributed under the Creative Commons Attribution License, which permits unrestricted use, distribution, and reproduction in any medium, provided the original work is properly cited.

With the increase of underground mining depth in coal mines, the distribution of stress fields in deep mining becomes more complex, and the stress localization characteristics are obvious. In order to obtain the local mechanical properties and energy evolution of sandstone, this article is based on the three-point bending experiment and combined with the localized failure theory to explore the evolution law of stress field, deformation field, and energy field of sandstone specimen under tensile stress during the three-point bending experiment. The results show that during the three-point bending test of sandstone, with the increase of the span of the three-point bending test, the peak stress at the characteristic point shows an increasing trend, and the peak stress has obvious regional characteristics. In the vertical direction, the peak stress at the characteristic points in the upper part of the neutral layer is larger, and the peak stress at the characteristic points in the lower part of the neutral layer is smaller. In the horizontal direction, the peak stress at the characteristic points in the near field is higher, and the peak stress at the characteristic points in the middle field and the far field is smaller. The stress field and the deformation field have a good corresponding relationship. The upper far-field peak strain tends to decrease with the increase of the span, and the upper near-field peak strain first decreases and then increases with the increase of the span. The lower near-field peak strain tends to decrease and then increase with increasing span, and the lower far-field peak strain fluctuates with increasing span. The energy field is dependent on the stress field and the deformation field, showing obvious regional characteristics. The energy storage and release capacity of the upper area are higher than those of the lower area. The overall performance of the loading energy storage, rebound energy release, and crack propagation energy release in different areas can be described as far field < mid-field << near field. The near-field energy at different spans presents the characteristics of two stages. When the span is between 140 mm and 150 mm, the near-field energy shows a rapid decreasing trend, and when the span is between 150 mm and 180 mm, the near-field energy presents an obvious increasing trend.

1. The Introduction

As an inhomogeneous and anisotropic elastic-plastic material, rocks constantly consume energy during the fracture process, resulting in irreversible plastic deformation and forming a process zone [1]. The plastic zone further evolves to form the initial crack, and the crack evolution process can be explored through the characteristics of rock deformation evolution. During the three-point bending test, the specimens are characterized by significant local deformation. Local failure is a concept that is the opposite of uniform failure [2]. Local failure is a phenomenon of small regional

failure occurring in a limited space. At the same time, local stress concentration or large local deformation is the precursor of local failure in coal and rock materials. Therefore, it is of great significance to analyze the initiation, propagation, and connection of three-point bending cracks in rocks from the perspective of the local deformation of rocks [3].

Domestic and foreign scholars have conducted a large number of three-point bending tests, and the deformation and crack evolution laws in different regions have been studied by Moiré interference, optical microscopy, ultrasonic, acoustic emission, and X-ray detection techniques [4–8], and the local deformation characteristics

and crack evolution laws during three-point bending of rocks have been obtained. Ningbo et al. studied the crack propagation, fracture morphology, medium strength, and acoustic emission response characteristics of coal and rock under bending load by three-point bending experiments [9]. Xingang et al. carried out a three-point bending test with prefabricated cracks, combined with numerical simulation software simulations. They found that the longer the crack length and the closer the inclination angle to $40^{\circ}\sim 60^{\circ}$, the more likely the coal and rock mass will fracture [10]. Hongguang et al. conducted the three-point bending test of concrete test blocks and combined it with the self-similarity characteristic function of the acoustic emission process. The self-similarity identification characteristics of the acoustic emission of concrete specimens during tensile fracture were determined on the basis of a given quantitative examination [11]. The same group of researchers also analyzed and calculated the variation of fractal dimensions associated with acoustic emission during the tensile fracture of the material through three-point bending experiments of concrete test block and obtained the fractal feature identification pattern of concrete test block at critical fracture in tension [12]. Zijiang et al. performed the three-point bending test on a half-disk using a straight slot-cut half-disk sample and a herring-shaped half-disk sample [13]. The principle of minimum energy consumption was analyzed by comparing the measured KIC values of the two slot-cutting methods. The reasons for the crack expansion into the bedding plane and the eventual formation of a rough fracture plane were derived. Funatsu et al. [14] studied the fracture toughness of sandstone at temperatures up to 200°C through a three-point bending test with a single notched circular bar and a three-point bending test of a semicircular bar. They paid attention to specimens with microscopic scales of 2–20 mm [15, 16]. Shaowei et al. determined the acoustic emission criterion of concrete tensile fracture by identifying acoustic emission characteristics at critical fracture of concrete under three-point bending [17]. Chaofu et al. investigated the influence of granite particle size on fracture mechanical behavior and acoustic emission characteristics through a three-point bending test combined with an acoustic emission three-dimensional positioning system [18].

Scholars have conducted many three-point bending tests with the help of acoustic emission and other technical means. Still, they have not explored the relationship between the local stress field, deformation field, and energy field from the perspective of three-point bending experiments. In this article, the acoustic emission test of the surface deformation field of the three-point bending specimen was conducted by a digital speckle measurement system during the three-point bending test. Based on the digital speckle correlation (XTDIC), the evolution characteristics of the surface deformation field of rock samples during damage and fracture were analyzed. The distribution characteristics and evolution law of stress field, deformation field, and energy field in the process of three-point bending test were analyzed.

2. Test Plan and Test Equipment

2.1. Sample Preparation. The compact and uniform sandstone samples were selected and processed into rectangular specimens of $50\text{ mm} \times 50\text{ mm} \times 200\text{ mm}$, with the dimensional error of the specimens within $\pm 0.3\text{ mm}$ and the verticality error less than 0.25° . The SonicViewer—SX ultrasonic testing system—is used to calibrate the samples one by one, and select samples with similar wave velocities to reduce the influence of the dispersion of sandstone samples on the test results. Rubber bands were glued on both ends of the specimens to fix the acoustic emission sensor probes, and speckle spraying was carried out on the side opposite to the strain gauges. In order to analyze the evolution characteristics of regional deformation during the loading process, five positions were selected on the left and right symmetrical planes with the longitudinal section of the loading as the center, and the transverse and longitudinal strain gauges were glued. The layout of sandstone specimens and strain gauges is shown in Figure 1.

2.2. Test Plan. The three-point bending test of sandstone was set up in five groups of tests with different lower fulcrum spans. The fulcrum spans were set to 180 mm, 170 mm, 160 mm, 150 mm, and 140 mm, and three specimens were carried out in each group of tests, as shown in Figure 2. At the beginning of the test, the press, acoustic emission, and digital speckle monitoring system were turned on and recorded simultaneously to ensure consistent monitoring time. The displacement control mode of 0.01 mm/s was adopted to load until the specimen was completely fractured.

The test device mainly consists of a stress loading system, dynamic strain gauge, acoustic emission, and digital speckle system. The composition of the test system is shown in Figure 3.

- ① The vertical load was applied to the sample by the electro-hydraulic servo system controlled by the taW-500 microcomputer. The load control accuracy of the test device was 0.001 kN , and the displacement control accuracy was 0.001 mm .
- ② The UT7160 static strain gauge was used to collect the strain at 20 points with a sampling frequency of 100 Hz and automatic temperature compensation using the $1/4$ bridge method.
- ③ The SH-II acoustic emission system was used to monitor the acoustic emission signals during loading. The frequency measurement range was $1\text{ KHz}\sim 3\text{ MHz}$, and the acoustic emission probe model was Nano30. The threshold value was 40 dB in a no-load state, and the sampling rate was 1 MSPS .
- ④ The XTDIC 3D digital speckle dynamic deformation measurement system was utilized to test the evolution characteristics of the surface deformation field. Speckles were sprayed on the surface of the sample. The digital granular system was used to track the changing characteristics of the feature points during the deformation process, supporting a measurement format of $4\text{ mm}\sim 4\text{ m}$.

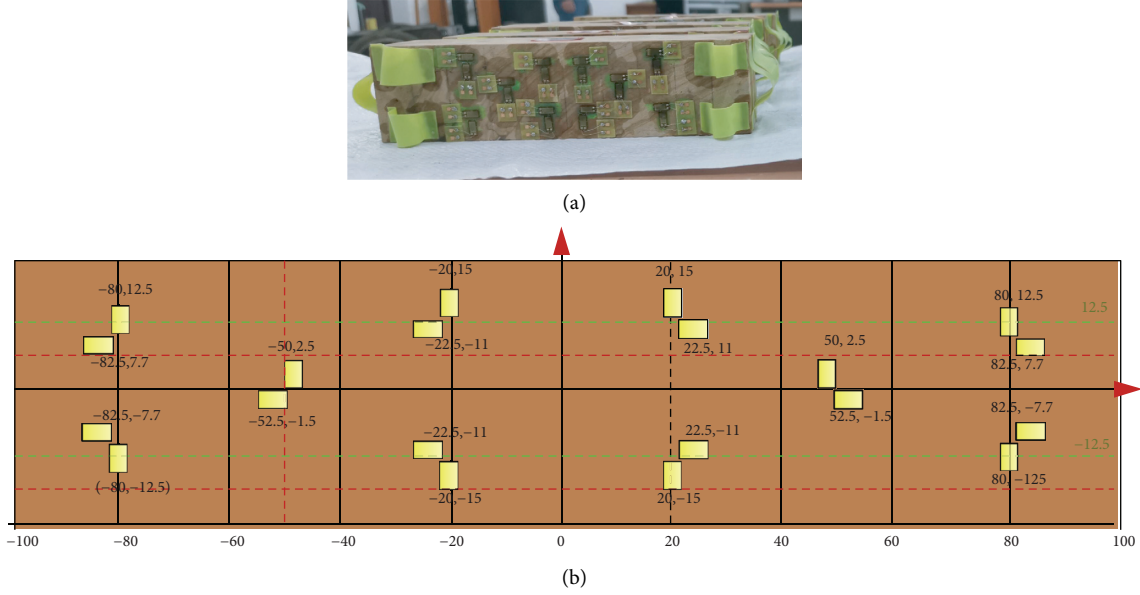


FIGURE 1: Sample preparation. (a) Typical samples. (b) Strain gauge.

3. Analysis of Distribution Characteristics of Stress Field

3.1. Stress Calculation at Feature Points. The stress in three-point bending is similar to that of a simply supported beam. The bending moment and shear force are generated under the action of the load. There are normal and shear stresses in any section cutting, and the normal stress is caused by the bending moment. Based on the theory of elasticity, the deformation of the plane curved beam is analyzed, and the stress at characteristic points can be obtained by combining the deformation geometry of the plane curved beam and Hooke's law. In reference [19], the geometric relations for the deformation of a simply supported beam are given. In combination with the basic definition of strain in physics, the strain is the ratio of shape variables to the original length and size, as follows:

$$\begin{aligned}\varepsilon &= \frac{(\rho + y)d\theta - \rho d\theta}{\rho d\theta} \\ &= \frac{y}{\rho}.\end{aligned}\quad (1)$$

In the three-point bending experiment, both the lower tensile deformation and the upper compression deformation are proportional to the coordinate y . As the neutral section is subjected to bending, the sandstone is subjected to stresses in only one direction: compressive stress in the upper part of the neutral layer and tensile stress in the lower part [20]. Based on the generalized Hooke's law,

$$\sigma = E\varepsilon. \quad (2)$$

Substitute formulae (1) into (2) to obtain:

$$\sigma = E \frac{y}{\rho}. \quad (3)$$

Formula (3) is for calculating the normal stress on the section, the normal stress on the section is proportional to the distance of the neutral layer, and all the stresses on the transverse section are equal, where y is the position from the neutral layer and ρ the curvature radius of the neutral layer,

$$F_N = \int_A \sigma dA = 0, \quad (4)$$

$$\begin{aligned}M_y &= \int_A z \sigma dA \\ &= 0,\end{aligned}\quad (5)$$

$$\begin{aligned}M_z &= \int_A y \sigma dA \\ &= 0.\end{aligned}\quad (6)$$

Substitute formulae (3) into (4) to obtain:

$$\begin{aligned}\int_A \sigma dA &= \frac{E}{\rho} \int_A y dA \\ &= 0.\end{aligned}\quad (7)$$

Since both E and ρ are nonzero values, the integral term must be equal to 0. A static distance of 0 indicates that the Z -axis passes through the centroid of the section.

Substitute formulae (3) into (5) to obtain:

$$\int_A z \sigma dA = \frac{E}{\rho} \int_A y z dA \quad (8)$$

$$= 0.$$

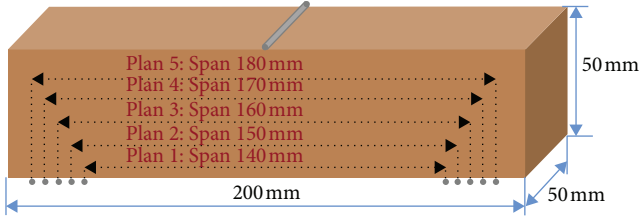


FIGURE 2: Fulcrum span arrangement.

The integral term is the moment of inertia of the Y-axis and Z-axis. Any section is symmetric along the Y-axis, so the moment of inertia of YZ is equal to 0, and formula (8) is equal to 0.

Substitute formulae (3) into (6) to obtain:

$$\begin{aligned} M_Z &= M \\ &= \int_A y \sigma dA \\ &= \frac{E}{\rho} \int_A y^2 dA, \end{aligned} \quad (9)$$

where the integral term is the moment of inertia (I_z) of Z-axis, and formula (9) can be transformed into

$$\frac{1}{\rho} = \frac{M}{EI_z}. \quad (10)$$

Substitute formulae (3) into (10) to obtain:

$$\sigma = \frac{M}{I_z} y. \quad (11)$$

where σ is the normal stress of a section, M is the bending moment of the corresponding section, I_z is the moment of inertia in the Z-axis, and y is the distance from the neutral layer. In order to calculate the distribution of normal stress on the cross section, it is necessary to calculate the bending moment and the moment of inertia. The bending moment of the three-point bending beam is determined by material mechanics. The calculation method of the bending moment and the moment of inertia of the rectangular section are calculated in the following equations, respectively:

$$M = \frac{Fx}{2} \left(0 \leq x \leq \frac{L}{2} \right), \quad (12)$$

$$I_z = \frac{bh^3}{12}. \quad (13)$$

According to the theoretical derivation of three-point bending normal stress formula (11), bending moment formula (12), and moment of inertia formula (13), combined with the load data of the press, the distribution law of stress field at any time can be obtained. The strain gauge layout points were taken as the analysis points, and the feature points were named as far field (upper left, lower left, upper right, and lower right), middle field (middle left and right), and near field (upper left, lower left, upper right, and lower right) according to the spatial position relationship, as shown in Figure 4.

3.2. Theoretical Analysis of Peak Stress. The curves of stress and displacement at feature points at different spans are shown in Figure 5. Due to the symmetry of the X-axis and Y-axis of the theoretical solution, the feature points contained in the upper right quarter region were selected for analysis.

With the increase of the span of the three-point bending test, the overall load of the specimen decreases, but the force arm of the characteristic point gradually increases with the increase of the span and the influence of the force arm on the stress is more obvious when the normal stress is calculated theoretically. The variation law of stress-displacement of different spans shows that the peak stress of the characteristic point increases with the increase of the span.

The peak stress characteristics of the characteristic points at different spans are shown in Figure 6. It can be seen that the peak stress has obvious regional characteristics, and the peak stresses vary greatly in different regions. The upper right (near-field) characteristic point is located in the upper middle area of the specimen, and the peak stress of the feature point is larger and in compression. The middle right (mid-field) characteristic point is located in the middle area on the right side of the specimen, which is roughly under the central layer, and the peak stress of the characteristic point is small and in tension. The upper right (far-field) characteristic point is located in the upper area on the right side of the specimen, which is far from the overall load loading line, and the peak stress of the characteristic point is small and in compression. From the above, it can be seen that the vertical direction affects the stress state in the specimen area, the upper area is in a compressed state, and the lower area is in a tensile state; the horizontal position affects the size of the peak stress in the specimen area, and the peak stress concentration in the middle area of the specimen is obvious.

4. Local Deformation Field Analysis Based on Strain Gauge

In the process of the sandstone three-point bending experiment, the stress concentration area eventually forms the main fracture zone. Studying the local deformation characteristics of the specimens has reference value for the critical state of overall instability. In terms of local monitoring, the electrical measurement method [7] was used to measure the deformation characteristics of different regions.

4.1. Deformation Characteristics of Feature Points. The bending moment generated by three-point bending mainly causes tensile strain below the neutral layer of sandstone and compressive strain above. The strain laws of the characteristic points of three-point bending in sandstone are similar for different spans. The strain characteristics of the characteristic points of sample s85-2 (with a span of 170 mm) were analyzed. Figure 7 shows the relationship curve between strain and time at the characteristic points of sample S85-2.

From the viewpoint of deformation state, in the early stage of loading, the upper part of the neutral layer (upper left and right upper middle and upper right and left upper)

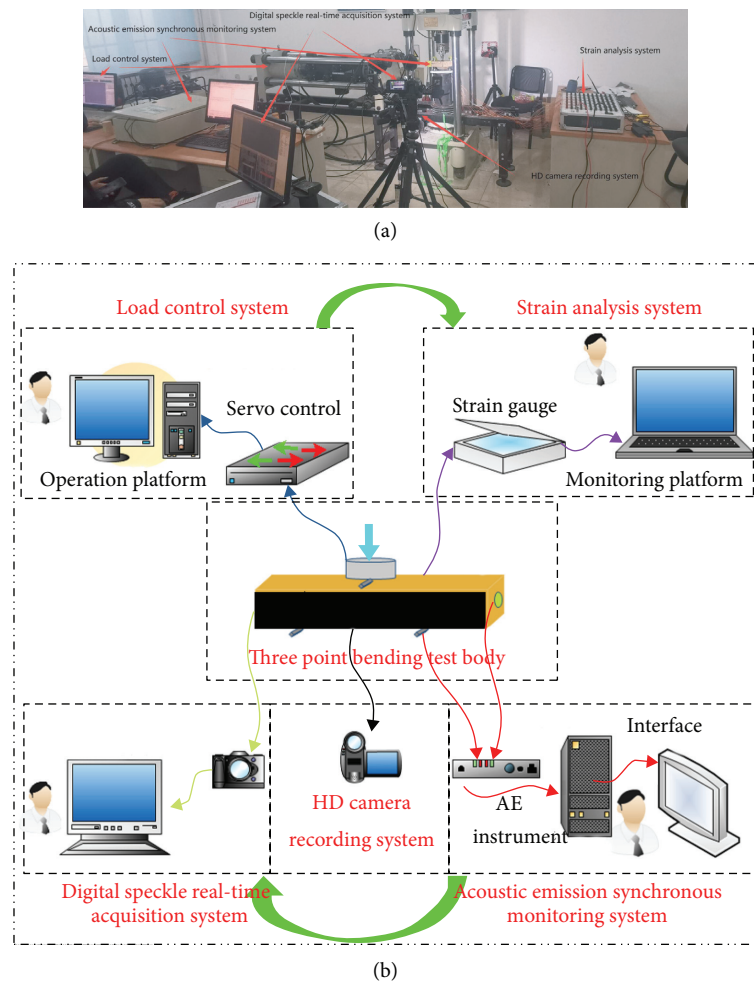


FIGURE 3: Test system. (a) Physical drawing of the experimental system. (b) Schematic diagram of the experimental system.

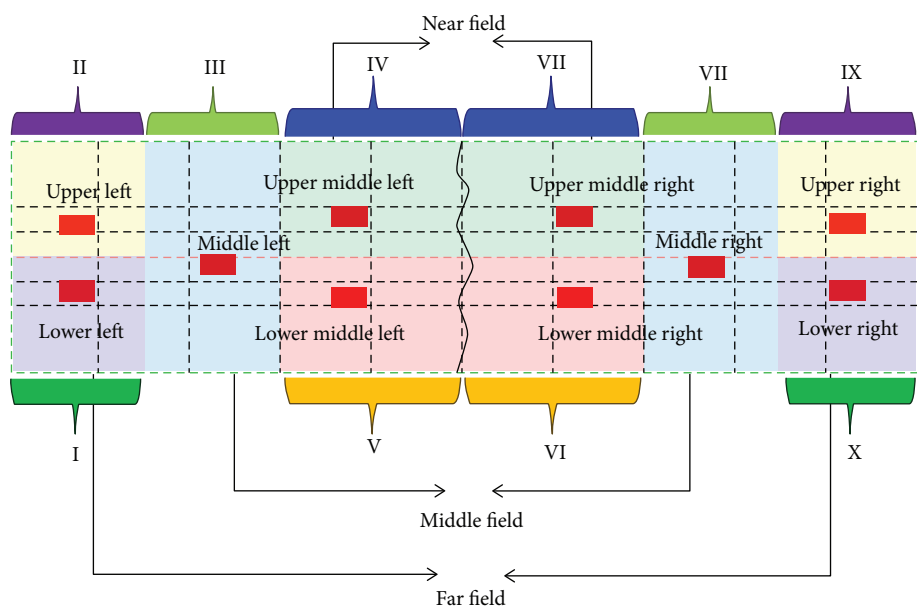


FIGURE 4: Setting of characteristic points in three.

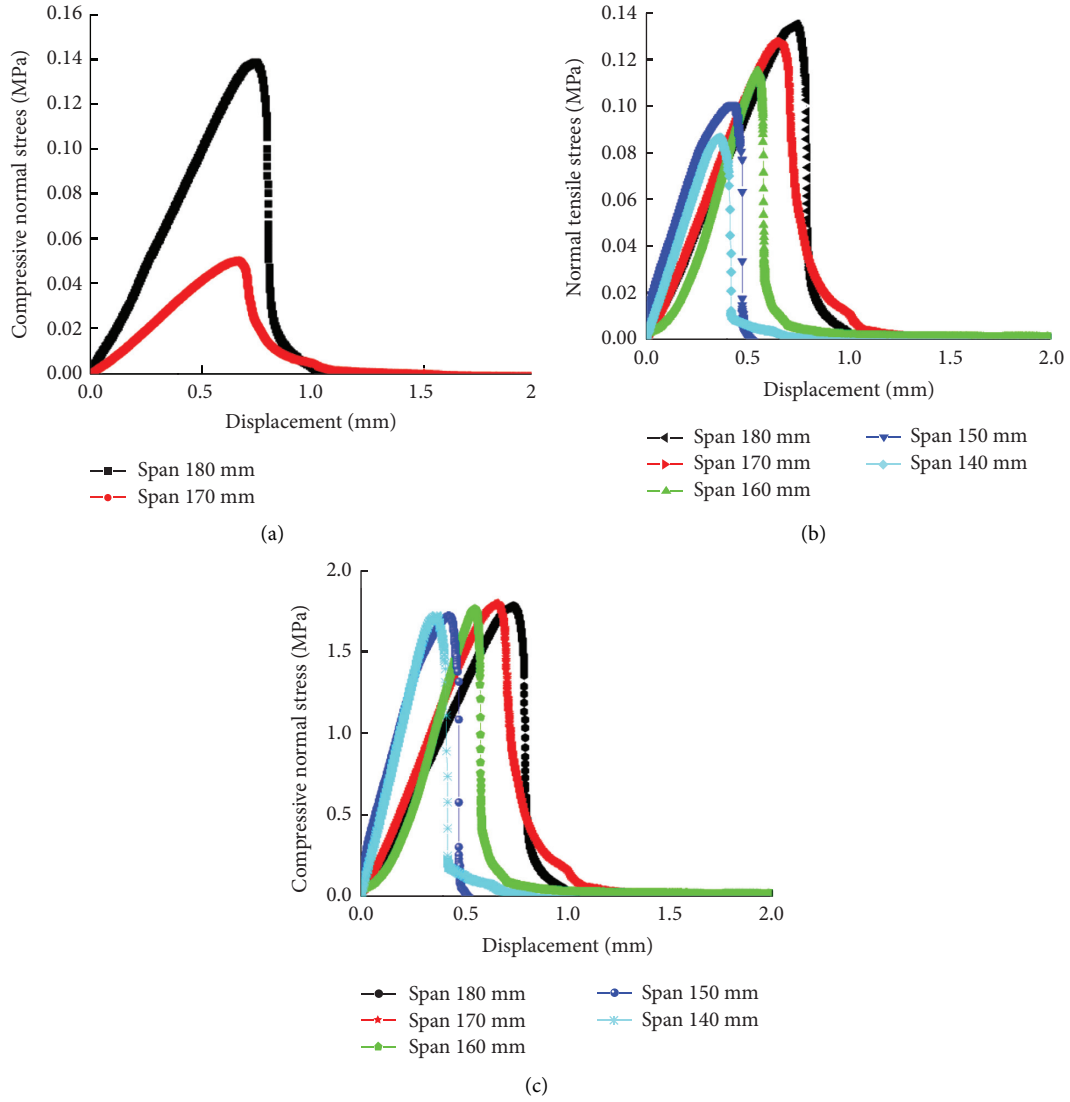


FIGURE 5: Stress-displacement curves of feature points with different spans. (a) Upper right feature point. (b) Middle right feature point. (c) Upper middle right feature point.

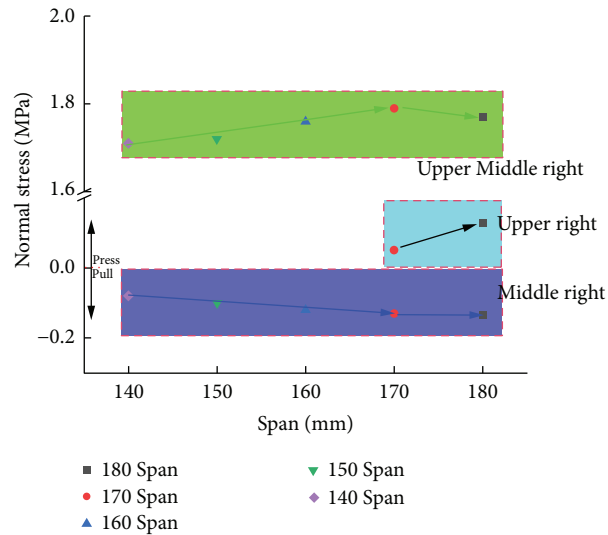


FIGURE 6: Peak stress at feature points with different spans.

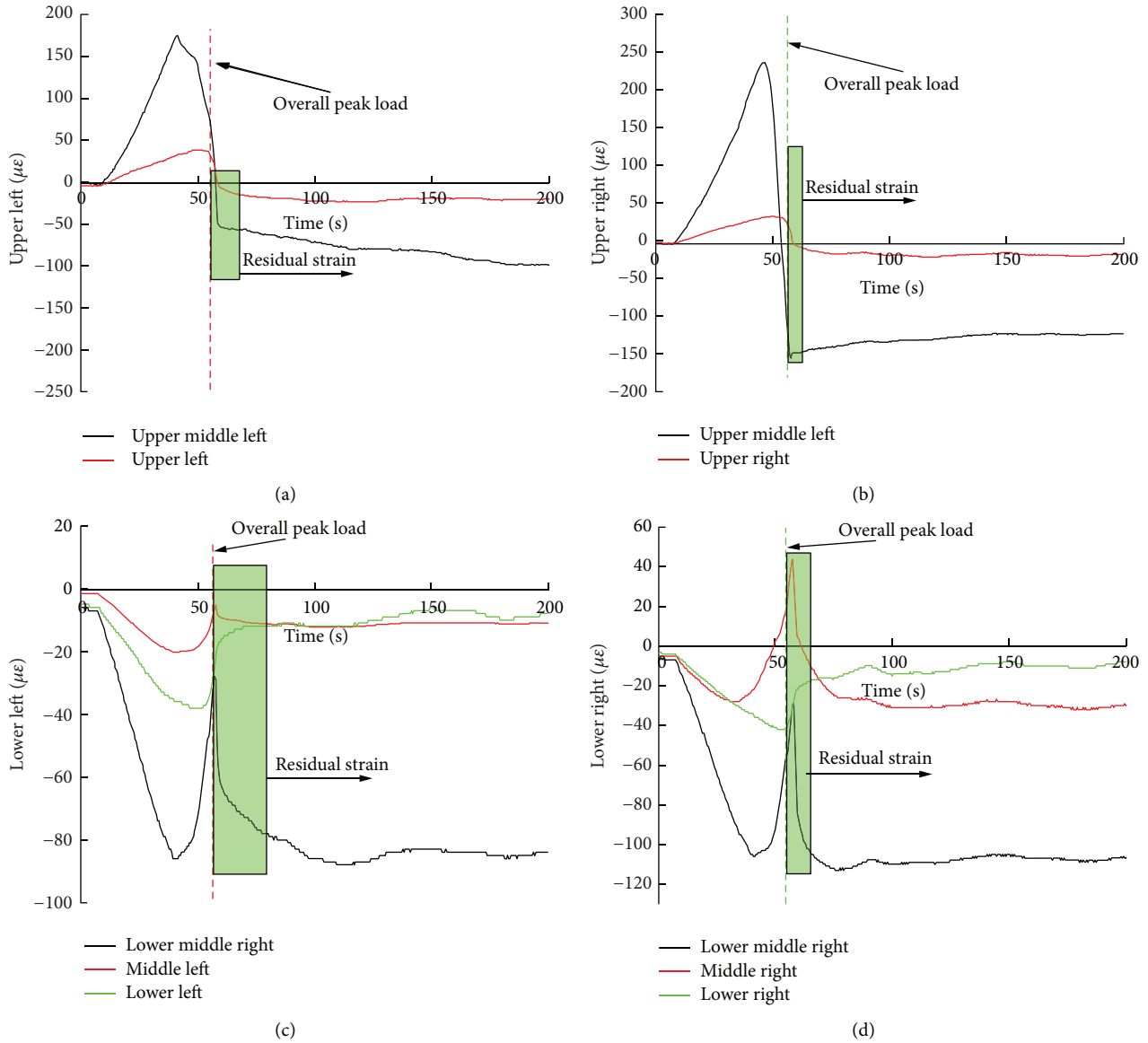


FIGURE 7: Strain-time curve at characteristic points of specimen S85-2. (a) Upper left area (b) Upper right area. (c) Lower left area. (d) Lower right area.

undergoes compression deformation. When the whole reaches the peak value, it gradually changes to tensile deformation and finally reaches the tensile state at the stage of residual strain. It is mainly due to the continuous upward movement of the neutral layer after the fracture occurs in the middle of the specimen, and the overall fracture leads to a tensile state in the whole field. In the process of loading to fracture, the lower part of the neutral layer (lower left and right middle and lower, right and left middle) has been deformed in tension. The deformation characteristics under the influence of the position are obvious, and the phenomenon of “jump” or “leap” appears locally. It is mainly the process of extension of the main control crack, resulting in the instantaneous transition release of stress at the characteristic point and the instantaneous adjustment of the spring back to the initial state.

4.2. Peak Strain at Feature Points. The peak strain can reflect the deformation characteristics and reflect the deformation and damage degree in the local area. The variation trend of peak strain at feature points under different spans is shown in Figure 8. The boundary point 0 is divided into compressive strain and tensile strain.

From the peak strain point of view, the analysis of the compressive peak strain in the upper part (upper left, upper left, upper right, and upper right) shows that the peak strain of the near field in the middle is larger than that of the far field when the span is 140 mm. With the increase of the span (150 mm, 160 mm), the peak strain in the middle field is approximately equal to the far-field strain in the small span. With the continuous increase of the span (170 mm, 180 mm), the peak strain in the near field is larger than that in the far field. The peak strain in the upper far field

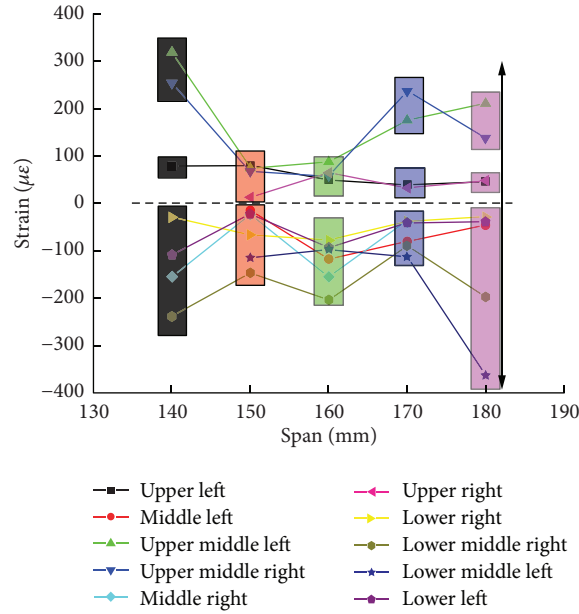


FIGURE 8: Peak strain at feature points with different spans.

decreases with the increase of the span, whereas the peak strain in the upper near field decreases first and then increases with the increase of the span.

For the lower part (lower left, middle left, lower left, lower right, lower right, middle right, and lower right), the analysis of tensile peak strain illustrates that the peak strains in the middle can be described as near field > middle field > far field when the span is 140 mm, indicating that the vertical direction has less influence than the horizontal direction. As the span increases (150 mm, 160 mm, 170 mm), the peak strains in the near field, middle field, and far field are closer and closer, but the peak strains in the near field are still larger than those in the far field, and the peak strains in the middle field are close to those in the far field. When the span is 180 mm, the peak strain in the near field is larger than that in the far field, and the peak strain in the middle field is basically the same as that in the far field. The peak strain in the lower near field decreases first and then increases with the increase of span, whereas the peak strain in the lower far field fluctuates with the increase of span, but remains at a low strain level all the time.

4.3. Peak Strain Normalization. Take a span of 170 mm as an example to illustrate the idea of time normalization. The peak load time of sample S85-2 is 54.825 s, and the corresponding peak strain-time of upper left, upper left middle, upper right, and upper right middle is 50.21 s, 40.72 s, 50.62 s, and 46.42 s. The corresponding time of peak strain is 49.89 s, 39.99 s, 40.36 s, 52.12 s, 35.12 s, and 40.72 s. The peak strain of the characteristic points all occurred before the fracture moment. Using the peak load moment of S85-2 as the normalized basis, the dimensionless values between 0 and 1 of each characteristic point were obtained. The calculation results were 0.92, 0.74, 0.92, 0.85, 0.91, 0.73, 0.74, 0.95, 0.64, and 0.74. In order to ensure the reliability of the

data, the peak strain-time of the same span is normalized and averaged. The normalized time curves of feature points of different spans are shown in Figure 9.

Among them, the strain peak appears on the left side of the 160 mm span after the overall load peak, so the normalization result is greater than 1. These data do not conform to the general law, so it is not within the scope of discussion. According to the aggregation characteristics and numerical values of the feature points, they are divided into three large intervals, in which less than 0.6 is the low feedback zone, 0.6–0.8 is the medium feedback zone, and 0.8–1 is the high feedback zone. Most of the feature points are in the high response zone, and the analysis of the far field (upper left, lower left, upper right, and lower right) shows that all of them are in the high feedback zone except the lower right with a span of 180 mm. Although there is some volatility in the far field with the change of span, the average values of normalized time are above 0.9. The mid-field (left and right) is mostly in the lower-middle feedback zone, indicating that the mid-field presents the earliest feedback. The near-field (upper left, lower left, and upper right, lower right) is in the high feedback low and high feedback high regions. Looking at the normalized time of feedback, it is found that the changing pattern is obvious; that is, the initial feedback comes from the mid-field, the middle feedback comes from the near field, and the late feedback comes from the far field. With the increase of span, the time feedback of feature points becomes more and more “loose” and the time span becomes larger, indicating that the small span is conducive to sensitivity aggregation and the obtained law is of reference value for prediction and early warning.

5. Evolution Law of Energy Field

During the loading process of the three-point bending experiment, the work of the press provides energy for the damage and destruction of the sandstone. There is a local

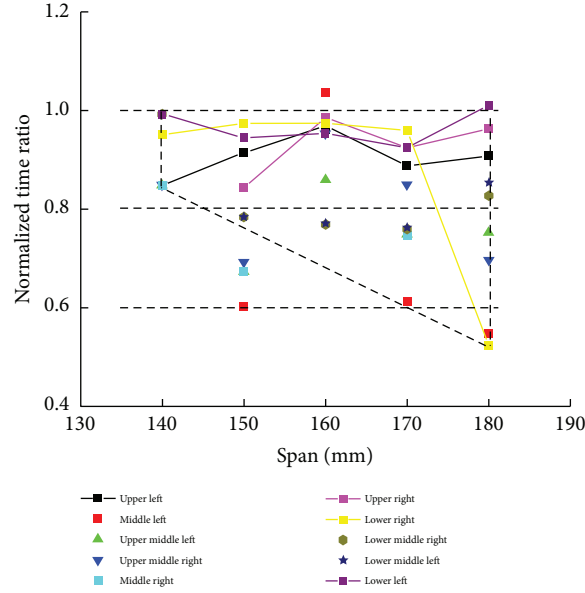


FIGURE 9: Variation rule of normalized time of feature points with different spans.

effect in the energy distribution; that is, the energy stored at the characteristic points is not the same, and especially the crack initiation, propagation, and penetration phases require continuous energy consumption. The energy stored in each region has to be “supplied” to the plastic zone fracture, resulting in the variability of the energy consumed in each region.

5.1. Energy Evolution Analysis of Feature Points. The energy evolution of the feature points presents three distinct stages (loading energy storage, rebound energy release, and crack propagation energy release). In the load energy storage stage, the local area and the entire specimen accumulate energy continuously. The energy accumulation in the local area is mainly influenced by the distribution characteristics of the stress and strain fields and the endpoint of loading energy storage, namely, when the characteristic point reaches its deformation and energy storage limit. As can be seen from the previous chapters, there are certain differences in the deformation peak size and occurrence time of the characteristic points in different regions, so there are large differences in the energy evolution of local regions. In the spring back and release energy stage, the cracks in the damage fracture zone are expanded from the bottom to the top. After the local characteristic points reach the limit of energy storage, the energy is consumed for the crack initiation and propagation in the damage fracture zone. In the phase of instantaneous crack propagation and energy release, the specimen occurs in the whole fracture. The energy release at the characteristic point is used for postpeak macrocrack connection and friction energy dissipation.

The energy characteristics of the local feature points of specimen S85-2 are shown in Figure 10. From the vertical direction, the loading energy storage and spring back release energy of the lower region are smaller than those of the upper region. The upper region is in compression, and its

deformation modulus is larger than that of the tensile region, which has a stronger load-bearing capacity. It has higher energy storage and release capacity than the lower region. The crack expansion release energy after the peak is at a relatively low energy level. According to the law of energy conservation, the input energy should be equal to the released energy. However, during the three-point bending experiment, the energy released in the local area is greater than the stored energy. The main reason is that after the local area reaches the energy storage limit, the external load still provides energy to the local area at the stage of rebound and release of energy.

In order to further analyze the energy evolution characteristics of different regions in the three-point bending test, the average energy values of feature points in the far-field, mid-field, and near-field regions were taken and the characteristic energy curves of different regions were drawn, as shown in Figure 11. From the horizontal direction, the energy in the near-field region is much larger than that in the far-field and the middle-field regions, and the energy evolution in the near-field region plays a leading role in the crack initiation, propagation, and coalescence of the specimen. The loading energy storage, spring back energy release, and crack propagation energy release in different areas can be described as far field < middle field < near field.

5.2. Analysis of Energy Distribution Law. In the process of three-point bending loading, energy is continuously accumulated inside the specimen under the action of load. As the load increases, a damage fracture zone is formed in the middle loading region of the specimen. Moreover, the initiation, expansion, and coalescence of cracks in the damage fracture zone consume energy. The elastic deformation mainly occurs in the area outside the damage fracture zone, and energy accumulation and release happen in the elastic

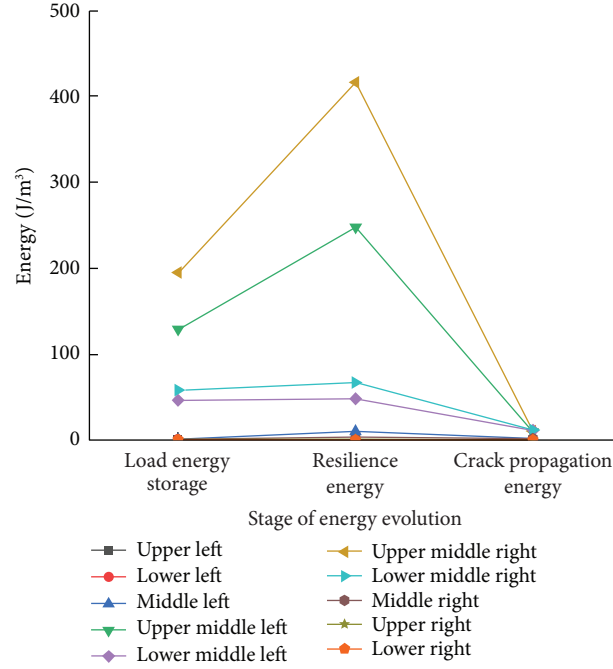


FIGURE 10: Energy characteristics of local feature points.

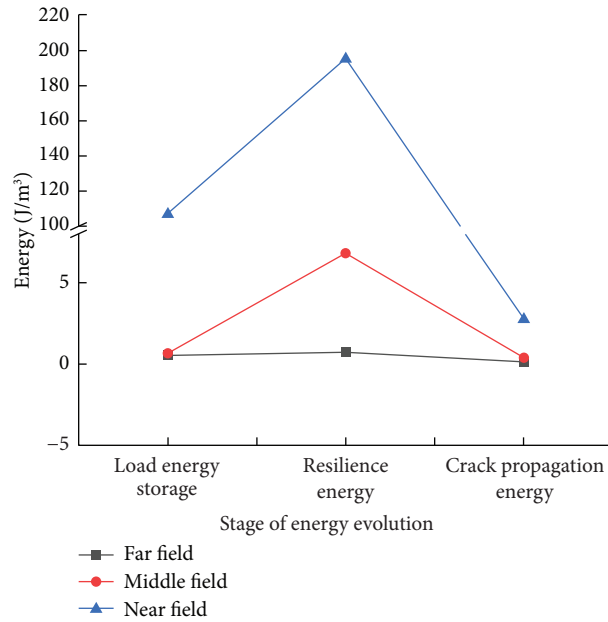


FIGURE 11: Energy characteristics of different regions.

deformation zone with the change of stress state. From the energy balance perspective, there is no energy dissipation in the elastic deformation zone under the ideal state. The energy released in the elastic deformation zone is used for the energy dissipation of crack initiation, propagation, and transfixion in the damage fracture zone.

The strain energy density per unit volume of the element body can be calculated according to the formula below, and its value is equivalent to the area under the stress-strain curve:

$$U^e = \frac{dW}{dV} = \int_0^{\varepsilon_1} \sigma d\varepsilon, \quad (14)$$

where U^e is strain energy density, J/m^3 .

During the three-point bending test, the fracture zone of the specimen occurred in the middle of the loading line region, and the elastic deformation happened outside the

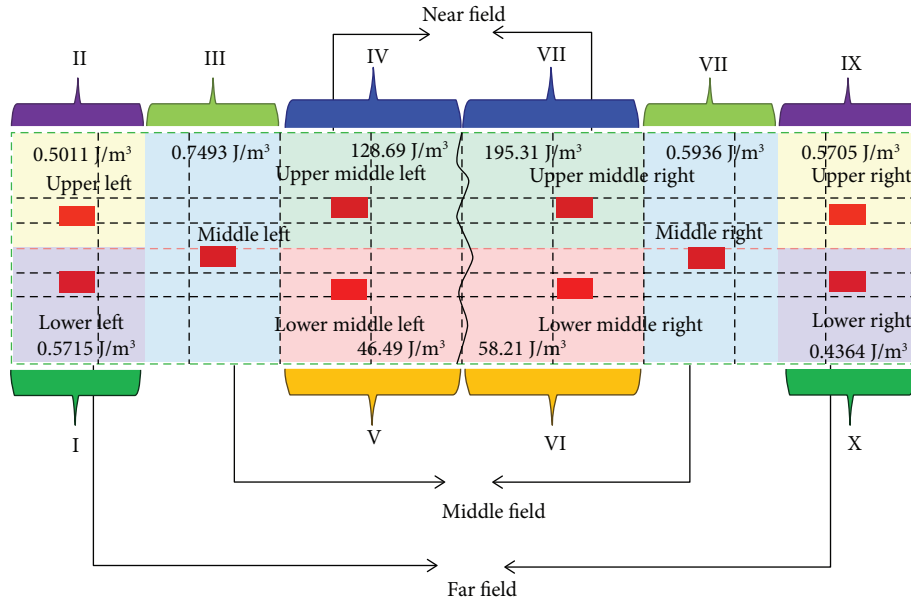


FIGURE 12: Elastic strain energy density at feature points.

fracture zone. Ten groups of strain gauges on the surface of the specimen were located in the elastic region, and the unit body in the elastic deformation region was approximately considered an ideal elastomer, and the above elastic strain energy calculation method was used to calculate the elastic strain energy at the characteristic point. According to the position relationship between the feature points and the loading line, the characteristic point area is divided into three regions: far field (upper left II, lower left I, upper right IX, and lower right X), middle field (middle left III and middle right VIII), and near field (upper left IV, lower left V, upper right VII, and lower right VI).

The calculation results of the elastic strain energy density of the characteristic points are shown in Figure 12. It can be seen that the elastic strain energy density of the near-field area is larger in the horizontal direction, and the strain energy density gradually decreases from the middle to both sides. Moreover, the closer the loading line is, the greater the stress and deformation of the element body is, and thus, the higher the elastic strain energy density is. Vertically, the upper area of characteristic points is bigger than the lower area of the strain energy density. The upper area of the unit cell is given priority to the compression state, and the lower area of the unit cell is given priority to the tensile state. The stresses and deformation of the cell in the compression state are larger than those of the tension state, resulting in a larger strain energy density of the upper part of the cell in the compression state. According to the energy density distribution characteristics of characteristic points, the energy distribution of the rock specimens has obvious accumulation characteristics; that is, there is little energy distribution in the middle and far fields, and the energy is mainly concentrated in the near-field region. The energy density is the largest in the area near the loading line.

6. Conclusion

- (1) The peak stresses have obvious regional characteristics, which vary greatly in different regions. The vertical direction affects the stress state in the specimen region. The upper region presents the compression state, whereas the lower region shows the tensile state. The horizontal position affects the size of the peak stress in the specimen region, and the peak stress concentration is obvious in the middle of the specimen. The peak stress in the near field is larger than that in the middle and far fields.
- (2) At 140 mm~180 mm span, the peak strain in the upper far-field decreases with the span, whereas the peak strain in the upper near-field decreases first and then increases with the increase of span. The peak strain in the lower near-field decreases first and then increases with the increase of span, whereas the peak strain in the lower far-field fluctuates with the increase of span but remains at a low strain level all the time. Whether in the upper or lower part, in the far, middle, or near fields, the peak strain values in the symmetric position are close. With the increase of span, the time feedback of feature points becomes more and more "loose," and the time span becomes larger and larger, indicating that a small span is conducive to sensitivity aggregation.
- (3) The loading energy storage and spring back release in the lower region are smaller than those in the upper region. The crack extension energy release after the peak is at a relatively low energy level. The energy released in the local area is greater than the stored energy during the experiment. The overall performance of loading energy storage, spring back energy release, and crack propagation energy release in

different areas can be described as far field < middle field << near field.

- (4) In the horizontal direction, the elastic strain energy density of the characteristic points in the near-field region is larger, and the strain energy density decreases. From the center to the vertical side, the strain energy density of the characteristic points in the upper region is significantly larger than that in the lower region. The cells in the upper region are mainly with the compressed state and the cells in the lower region are mainly with the tensile state. The stress and deformation of the cells in the compressed state are larger than those in the tensile state. The energy distribution of the rock specimens has obvious accumulation characteristics; that is, there is little energy distribution in the middle and far fields, and the energy is mainly concentrated in the near-field region.

Data Availability

The data used to support the findings of this study are available from the corresponding author upon request (e-mail: 19140270@qq.com).

Conflicts of Interest

The authors declare that they have no conflicts of interest.

Acknowledgments

This study was supported by the Outstanding Young Talents Project, which is supported by the Central Government for the Reform and Development of Local Universities (2020YQ13).

References

- [1] X. Wang, *Deformation, Failure and Stability of Strain-Softening Materials: Analytical and Numerical Analyses*, Liaoning Technical University, Fuxin China, 2006.
- [2] W. Ji, P. Pan, S. Miao, S. S. Fang, and P. D. Meng, "Fracture characteristics of two types of rocks based on digital image correlation," *Rock and Soil Mechanics*, vol. 37, no. 8, pp. 2299–2305, 2016, in Chinese.
- [3] W. Liangbao and M. Jiang, *Experimental Mechanics*, vol. 33, no. 3, pp. 410–418, 2018.
- [4] L. Cedolin, S. P. Dei, and I. Iori, "Experimental Determination Of The Fracture Process Zone In Concrete," *Cement and Concrete Research*, vol. 13, no. 4, pp. 557–567, 1983.
- [5] J. F. Labuz, S. P. Shah, and C. H. Dowding, "Experimental Analysis Of Crack Propagation In Granite," *International Journal of Rock Mechanics and Mining Science & Geomechanics Abstracts*, vol. 22, no. 2, pp. 85–98, 1985.
- [6] J. F. Labuz, S. P. Shah, and C. H. Dowding, "The Fracture Process Zone In Granite: Evidence And Effect," *International Journal of Rock Mechanics and Mining Science & Geomechanics Abstracts*, vol. 24, no. 4, pp. 235–246, 1987.
- [7] A. Maji and S. P. Shah, "Process Zone And Acoustic-Emission Measurements In Concrete," *Experimental Mechanics*, vol. 28, no. 1, pp. 27–33, 1988.
- [8] K. Otsuka and H. Date, "Fracture Process Zone In Concrete Tension Specimen," *Engineering Fracture Mechanics*, vol. 65, no. 2-3, pp. 111–131, 2000.
- [9] Z. Ningbo, S. R. Enliang, Z. Shankun et al., "Investigation On Cracking Features Of Different Rock Under The Bending Load," *Journal of China Coal Society*, vol. 45, no. S2, pp. 671–681, 2020.
- [10] N. Xin-gang, Z. Yong-jiang, and C. Jian-jun, "Influence analysis of open crack on fracture characteristics of coal and rock mass," in *Proceedings of the 10th National Mining Academic Conference*, pp. 11–17, Topic 2: Safety Technology and Engineering, Ordos, China, 2015.
- [11] J. I. Hongguang and C. Meifeng, "Recognition Characterization Of Acoustic emission Self - Similarity In Concrete Fracturing," *Chinese Journal of Rock Mechanics and Engineering*, vol. 18, no. 2, pp. 157–160, 1999.
- [12] J. I. Hongguang, W. Jicai, S. Xiaoyun et al., "Fractal characteristics of ae process of concrete material and application to the fracture analyses," *Chinese Journal of Rock Mechanics and Engineering*, vol. 20, no. 6, pp. 801–804, 2001.
- [13] Z. J. Zhao, D. A. Liu, Z. D. Cui, and G. Han, "Experimental Study Of Determining Fracture Toughness KIC Of Shale By Semi-Disk Three-Point Bending," *Rock and Soil Mechanics*, vol. 39, no. S1, pp. 258–266, 2018.
- [14] T. Funatsu, M. Seto, H. Shimada, K. Matsui, and M. Kuruppu, "Combined Effects Of Increasing Temperature and Confining Pressure On The Fracture Toughness Of Clay Bearing Rocks," *International Journal of Rock Mechanics and Mining Sciences*, vol. 41, no. 6, pp. 927–938, 2004.
- [15] W. Yang, *Macro-micro fracture mechanics*, National Defence Industry Press, Beijing, China, 1995, in Chinese.
- [16] J. P. Zuo, H. P. Xie, and H. W. Zhou, "Investigation On Meso-Failure Behavior Of Sandstone Under Thermal-Mechanical Effects Based On High Temperature SEM," *Science China Physics, Mechanics and Astronomy*, vol. 55, no. 10, pp. 855–862, 2012.
- [17] H. Shaowei, L. Jun, and F. Xiangqian, "Study On Acoustic Emission Technique For Normal Concrete Fracture Test," *Journal of Hydroelectric Engineering*, vol. 30, no. 6, pp. 16–19, 2011.
- [18] D. Chaofu, L. Jianfeng, C. Liang, and Y. Li, "Fracture mechanical behaviors and acoustic emission characteristics of Beishan Granite With Different Particle Sizes," *Rock and Soil Mechanics*, vol. 7, no. 8, pp. 2313–2320, 2016.
- [19] H. Dai, *Mechanics of Materials*, Hunan University Press, Hunan, China, 2014.
- [20] Z. Xu, *Elastic Mechanics*, Higher Education Press, Beijing, China, 4TH edition, 2013.